PEPSI deep spectra

III. Chemical analysis of the ancient planet-host star Kepler−444[⋆]

C. E. Mack III[1], K. G. Strassmeier[1], I. Ilyin[1], S. C. Schuler[2], F. Spada[1], and S. A. Barnes[1]

[1] Leibniz-Institute for Astrophysics Potsdam (AIP), An der Sternwarte 16, 14482 Potsdam, Germany
    e-mail: kstrassmeier@aip.de
[2] University of Tampa, Tampa, FL 33606, USA
    e-mail: sschuler@ut.edu

ABSTRACT

Context. With the Large Binocular Telescope (LBT), we obtained a spectrum with PEPSI, its new optical high-resolution échelle spectrograph. The spectrum has very high resolution and a high signal-to-noise (S/N) and is of the K0V host Kepler−444, which is known to host five sub-Earth-sized rocky planets. The spectrum has a resolution of $R \approx 250\,000$, a continuous wavelength coverage from 4230 Å to 9120 Å, and an S/N between 150–550:1 (blue to red).
Aims. We performed a detailed chemical analysis to determine the photospheric abundances of 18 chemical elements. These were used to place constraints on the bulk composition of the five rocky planets.
Methods. Our spectral analysis employs the equivalent-width method for most of our spectral lines, but we used spectral synthesis to fit a small number of lines that required special care. In both cases, we derived our abundances using the MOOG spectral analysis package and Kurucz model atmospheres.
Results. We find no correlation between elemental abundance and condensation temperature among the refractory elements ($T_C > 950$ K). In addition, using our spectroscopic stellar parameters and isochrone fitting, we find an age of 10 ± 1.5 Gyr, which is consistent with the asteroseismic age of 11 ± 1 Gyr. Finally, from the photospheric abundances of Mg, Si, and Fe, we estimate that the typical Fe-core mass fraction for the rocky planets in the Kepler−444 system is approximately 24%.
Conclusions. If our estimate of the Fe-core mass fraction is confirmed by more detailed modeling of the disk chemistry and simulations of planet formation and evolution in the Kepler−444 system, then this would suggest that rocky planets in more metal-poor and α-enhanced systems may tend to be less dense than their counterparts of comparable size in more metal-rich systems.

Key words. stars: abundances – stars: atmospheres – stars: late-type – stars: activity – planetary systems

1. Introduction

The chemical composition of a planet-hosting star is known to influence the architecture of its planetary system (Dawson & Murray-Clay 2013; Adibekyan et al. 2013; Beaugé & Nesvorný 2013). Statistical surveys of exoplanet host stars show that Jupiter-like giants are preferentially formed around metal-rich stars (Fischer & Valenti 2005; Udry & Santos 2007; Ghezzi et al. 2010), while smaller planets appear to be less selective (Sousa et al. 2011; Buchhave et al. 2012, 2014; Schuler et al. 2015). This has been interpreted as evidence for the prevalence of the core accretion model of planet formation (Ida & Lin 2004; Mordasini et al. 2009). However, it should be noted that recent work (Nayakshin 2017) has shown that formation by gravitational instability via the tidal downsizing

model can also reproduce the observed correlation between giant planets and host star metallicity.

On the other hand, the formation of terrestrial planets does not seem to prefer iron-rich environments and succeeds with similar frequency around stars of various metallicities. Nevertheless, recent studies have hinted at some chemical preference for terrestrial planets. In particular, Adibekyan et al. (2015) showed that metal-poor planet hosts tend to have a higher [Mg/Si] ratio than metal-poor stars without detected planets. In addition, Dressing et al. (2015) found that for a small sample of Kepler planets with well-known masses and radii, planets with masses $<6M_\oplus$ are likely to have very similar iron-to-magnesium silicate ratios, and therefore follow a single mass-radius relationship. Furthermore, Santos et al. (2015) used a simplified chemical network based on detailed simulations performed by other teams (Lodders 2003; Seager et al. 2007) to estimate the Fe-core mass fraction of a subset of the rocky planets from the Dressing et al. sample: Kepler−10b, Kepler−93b, and CoRoT−7b. Santos et al. (2015) found that their simplified model predicted Fe-core mass fractions of ∼30% for all three planets. In this paper, we aim to use the same simplified model to estimate the Fe-core mass fraction for the five rocky planets orbiting the Kepler host star Kepler−444.

The discovery of a multi-planet system around Kepler−444 (KOI-3158, HIP 94931) was reported in Campante et al. (2015).

Their photometric analysis revealed five transiting planets with radii between those of Mercury and Venus and orbits within 0.1 AU of the star (i.e., within the orbit of Mercury). Perhaps even more astounding is the old age of the host star, 11.2 ± 1.0 Gyr, which Campante et al. determined from asteroseismology. Furthermore, their spectroscopic analysis of a Keck/HIRES spectrum ($R \approx 60\,000$, $S/N \approx 200$) yielded $T_{\rm eff} = 5046$ K and $\log g = 4.6$, together with sub-solar abundances of Fe as well as Si and Ti (two α-elements), leading to a moderately high [α/Fe] index of 0.26 dex. Thus, it appears that (low-mass) planet formation has been ongoing shortly after the Universe was created and that the chemical composition of the prestellar material did not have to be metal rich.

In order to perform a detailed chemical abundance analysis of Kepler$-$444, we obtained high-resolution, high signal-to-noise (S/N) spectra with the optical high-resolution échelle spectrograph PEPSI (Strassmeier et al. 2015), which was recently commissioned at the 11.8 m Large Binocular Telescope (Hill et al. 2012). We performed our detailed analysis in order to ascertain the degree to which the photospheric abundances of the host star can place constraints on the bulk compositions of the planets.

In Sect. 2 we describe the observations and the spectrograph, while Sect. 3 describes the data analysis. Section 4 presents our results, and in Sect. 5 we discuss the implications of these results and suggest possible research avenues for future work. Finally, in Sect. 6, we summarize our findings and conclusions.

2. Observations

High-resolution $R \approx 250\,000$ spectra of Kepler$-$444 were obtained with the Potsdam Echelle Polarimetric and Spectroscopic Instrument (PEPSI; Strassmeier et al. 2015) at the 2×8.4 m LBT. PEPSI is an asymmetric fiber-fed white-pupil échelle spectrograph with two arms (blue and red) that typically cover the wavelength range 383–907 nm. The instrument is stabilized in a pressure- and thermally controlled chamber and is fed by three pairs of octagonal fibres per telescope. The different core diameters of the fibres and their respective image-slicer width set the three different resolutions of the spectrograph (43 000, 120 000, and 250 000). The 250 000-mode was used for the spectra in this paper and is made possible with a seven-slice image slicer and a 100 μm fibre through a projected sky aperture of 0.74″, comparable to the median seeing of the LBT site. The actual resolution varies with wavelength and depends on the position of the échelle order on the CCD and on the focus position. It is generally lowest at the order edges, in particular in the blue arm, and highest near the blaze in the red arm at 7000 Å. It ranges from an average of 220 000 in the blue arm to an average of 250 000 in the red arm. The projected image slices are covered in the cross-dispersion direction by 12 pixels per slice. Two $10.3k \times 10.3k$ STA1600LN CCDs with 9 μm pixels record a total of 92 échelle orders.

PEPSI can be used either with sky fibers for simultaneous sky and target exposures or with light from a stabilized Fabry-Pérot etalon (FPE) for simultaneous fringe and target exposures for precise radial velocities. All spectra in this paper were taken in target+target mode, that is, no simultaneous sky or FPE exposures, only two simultaneous target spectra, one from each of the LBT unit telescopes. At the time when the present spectra were obtained, we had just repositioned the cross dispersers and ended up with an extra échelle order in the redmost unit. Because of (telescope) time constraints, we were unable to use the bluest

cross disperser at all. Therefore our Kepler$-$444 spectra cover the wavelength range 4230–9120 Å, with an average dispersion that varies from 7 mÅ per pixel in CD I to 19 mÅ per pixel in CD VI.

The data we study here were taken during spectrograph commissioning, and thus full instrument performance was not achieved yet (see paper I and paper II; Strassmeier et al. 2018a,b for details). Observations were conducted on May 23, and 24, 2015. Exposure times of 7, 10, 20, and 30 min were chosen, depending upon wavelength range, seeing, and time availability. Table 1 summarizes the observing log. Basic data reduction followed the procedures laid out and described in detail in paper I.

After optimal extraction and wavelength calibration, the one-dimensional spectra were coadded to build the single "deep spectrum" in Table 1. Altogether, the deep spectrum was assembled from seven individual spectra in CD II, five in CD III, four in CD IV, three in CD V, and four in CD VI. Each pixel of each spectrum was weighted according to its inverse variance from the optimal extraction and was optimally resampled before adding. We also note that each individual spectrum is two spectra in our case because the LBT is in fact a combination of two telescopes. At one occasion on May 24, 09:46UT, the DX M1 mirror cell panicked during integration, and the spectrum from one side was lost. Figure 1a shows the full spectrum. A portion of it spanning the wavelength region $\lambda6140$-$\lambda6170$ is shown in Fig. 1b.

3. Analysis

The chemical abundances (relative to solar) of 18 elements were derived from the deep spectrum of Kepler$-$444. The 2014 version of the local thermal equilibrium (LTE) spectral analysis package MOOG (Sneden 1973) was used to perform the spectral analysis. The abundances were derived from measurements of the equivalent widths (EWs) of atomic lines using the SPECTRE analysis package (Fitzpatrick & Sneden 1987). By requiring excitation and ionization balance of the Fe I and Fe II lines, we were able to derive the stellar parameters: $T_{\rm eff}$, $\log g$, [Fe/H], and ξ (microturbulence). The line lists for the wavelength regions encompassing each element were taken from the Vienna Atomic Line Database VALD; Piskunov et al. (1995); Kupka et al. (1999). Abundances are always given relative to solar[1]. The solar spectrum that we used is the grand average from paper I (Strassmeier et al. 2018a).

The carbon abundances were derived from the C_2 Swan system features at $\lambda5086$ and $\lambda5135$ using the *synth* driver in MOOG to synthetically fit them by eye. In addition, the EWs of three high-excitation C I lines were measured: $\lambda5052.17$, $\lambda5380.34$, and $\lambda7113.18$. Abundances were derived from these EW measurements using the MOOG *abfind* driver.

The two components of the C_2 Swan system yield relative abundances that are identical, that is, [C/H] = -0.56. However, the high-excitation C I lines yield discrepant relative abundances of [C/H] = -0.31, -0.07, $+0.22$, respectively. Previous LTE analyses of high-excitation lines, such as the O I triplet at $\lambda7775$ Å (e.g., Schuler et al. 2004, 2006; Ramírez et al. 2014), have found that the abundances derived from high-excitation lines increase with decreasing $T_{\rm eff}$ for stars with $T_{\rm eff} \le 5\,400$ K. For the high-excitation C I lines in particular, Schuler et al. (2015) found that these lines also give abundances that are higher by $\sim$0.16 dex than the C_2 Swan lines for Kepler–37, a star with $T_{\rm eff}$ of 5 400 K.

---

[1] $[X/H] = \log(N_X)_{\rm star} - \log(N_X)_{\rm Sun}$ with $\log(N_X) = \log(N_X/N_{\rm H}) + 12$.

Table 1. Spectra observed with PEPSI.

Date (UT)	Time	Air mass	Seeing ('')	Exp. (min)	CD	λ (nm)	S/N[a]	CD	λ (nm)	S/N[a]
2015, May 24	08:19	1.1	0.9	20	III	480–544	85	V	628–742	156
	08:40	1.1	0.9	20	III	480–544	98	V	628–742	181
	09:24	1.1	0.9	20	III	480–544	99	V	628–742	202
	09:46	1.1	0.9	20	II	423–480	75	…	…	…
	10:14	1.1	0.9	20	II	423–480	92	VI	742–912	262
	10:35	1.1	0.9	7	II	423–480	54	VI	742–912	156
2015, May 25	03:51	1.2	0.9	20	II	423–480	98	IV	742–912	177
	07:58	1.2	0.8	30	III	480–544	142	VI	742–912	247
	08:29	1.2	0.8	30	III	480–544	164	VI	742–912	284
	09:02	1.1	1.0	10	II	423–480	60	IV	544–628	131
	10:32	1.1	1.0	30	II	423–480	133	IV	544–628	261
	11:03	1.1	1.0	30	II	423–480	134	IV	544–628	265
Deep spectrum					I	…	…	IV	544–628	300–500
					II	423–480	150–300	V	628–742	250–300
					III	480–544	200–300	VI	742–912	550–300

Notes. [a]The S/N for the individual spectra is given for the central wavelength of each cross disperser (CD). The S/N for the deep spectrum is given for the full wavelength range as indicated.
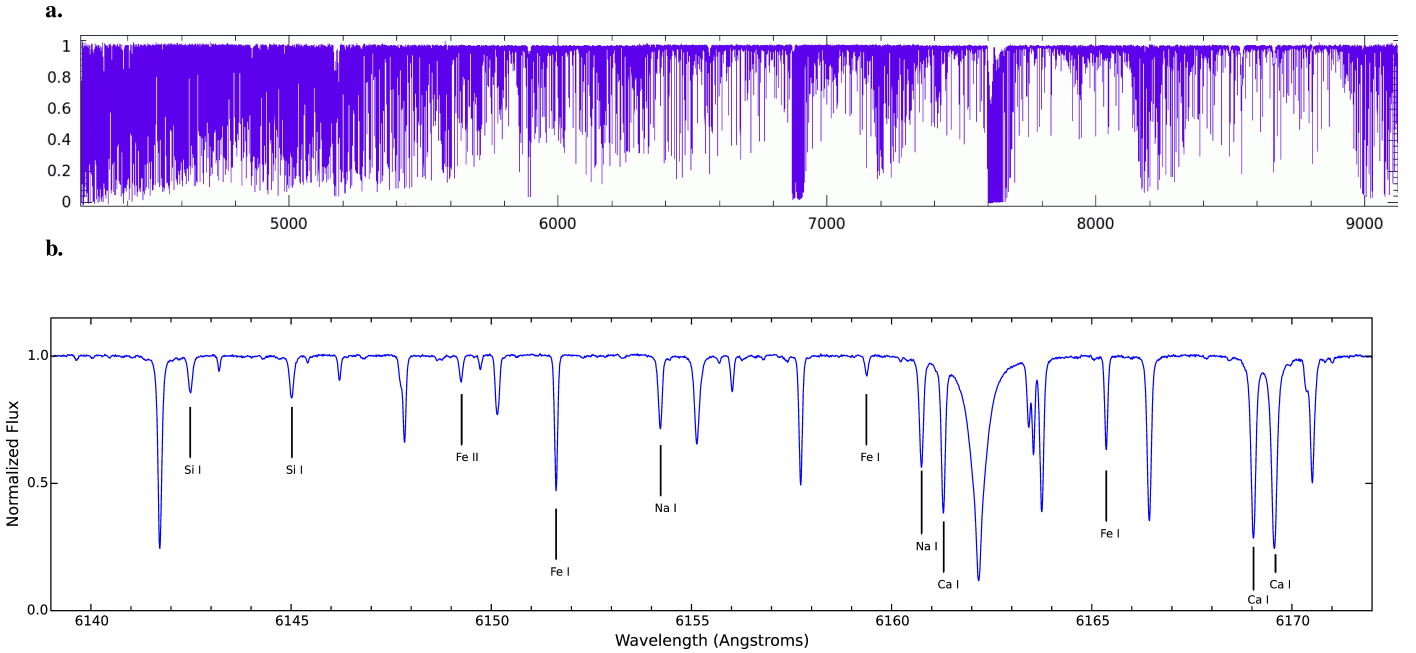
a.

b.

Fig. 1. Kepler−444 deep spectrum. *a)* Full spectral region between 4230–9120 Å. *b)* Spectral region between ~6140 Å and ~6170 Å. A selection of the lines measured in this region is labeled.

Our C abundances for Kepler–444 seem to follow this same pattern, suggesting that in this cool star, the C I lines do not provide reliable abundances. We therefore adopt the abundance determined from the C_2 Swan system as the carbon abundance here.

For the oxygen abundances, four spectral lines were analyzed: the forbidden line at λ6300.34, and the near-infrared triplet at λ7771.94, λ7774.17, and λ7775.39. The forbidden line was analyzed by measuring the equivalent width and using the MOOG *blends* driver to account for known blends with spectral lines from other elements, in particular, the known blend with an Ni line. For the near-infrared triplet, we measured their equivalent widths and used the standard MOOG *abfind* driver. We then corrected the near-infrared triplet abundances for NLTE effects using the corrections from Takeda (2003). The forbidden line and the near-infrared triplet yielded relative abundances that agree reasonably well: [O/H] = −0.12 and −0.09, respectively. More recently, Amarsi et al. (2016) provided three-dimensional (3D) NLTE corrections for 1D LTE abundances for the temperature range 5 000–6 500 K. Applied to our measurements, this corrects to abundances of −0.13 and −0.11 for the forbidden and the near-infrared triplet, respectively. Therefore we simply

Table 2. Stellar parameters and abundances.

Kepler−444	
T_{eff} (K)	$5,172 \pm 75$
$\log g$ (cgs)	4.56 ± 0.18
ξ (km s^{-1})	1.64 ± 0.37
[C/H]	$-0.56 \pm 0.000^a \pm 0.03^b$
[O/H]^c	$-0.11 \pm 0.027 \pm 0.12$
[Na/H]	$-0.44 \pm 0.055 \pm 0.08$
[Mg/H]	$-0.27 \pm 0.033 \pm 0.05$
[Al/H]	$-0.19 \pm 0.014 \pm 0.05$
[Si/H]	$-0.37 \pm 0.022 \pm 0.04$
[K/H]	$-0.38 \pm \ldots \pm 0.13$
[Ca/H]	$-0.53 \pm 0.020 \pm 0.10$
[Sc/H]	$-0.34 \pm 0.011 \pm 0.08$
[Ti/H]	$-0.27 \pm 0.036 \pm 0.11$
[V/H]	$-0.18 \pm 0.024 \pm 0.11$
[Cr/H]	$-0.46 \pm 0.006 \pm 0.07$
[Fe/H]	$-0.52 \pm 0.011 \pm 0.12$
[Mn/H]	$-0.61 \pm 0.030 \pm 0.10$
[Co/H]	$-0.33 \pm 0.015 \pm 0.06$
[Ni/H]	$-0.50 \pm 0.013 \pm 0.05$
[Zn/H]	$-0.41 \pm 0.004 \pm 0.08$
[Y/H]	$-0.51 \pm \ldots \pm 0.12$

Notes. Adopted solar parameters (Cox 2000): $T_{\text{eff}} = 5\,777$ K, $\log g = 4.44$, and $\xi = 1.38$ km s^{-1}. $^{(a)}$The uncertainty in the mean. For C, both spectral lines yielded the same abundance; for K and Y, the abundance was derived from a single spectral line; and for Co, all the spectral lines yielded the same abundance, except for one that differed by 0.01 dex. $^{(b)}$The quadratic sum of the uncertainty in the mean and the uncertainties due to T_{eff}, $\log g$, and ξ. $^{(c)}$Corrected for NLTE effects, see text.

averaged these abundances and adopted an [O/H] abundance of -0.11. We note that significant disagreement between the near-infrared triplet and forbidden line relative abundance has been seen before in open cluster dwarf stars with spectral types similar to Kepler−444 (Schuler et al. 2006). However, there is some evidence that the discrepancy between these two [O/H] indicators may decrease with age, which we discuss further in Sect. 5.1.

For V and Co, in order to account for possible hyper-fine structure (hfs) effects (Prochaska & McWilliam 2000), we used the MOOG *blends* driver on specific spectral lines: the V I lines at $\lambda6090.21$ and $\lambda6111.65$, and the Co I lines at $\lambda5301.04$, $\lambda5352.04$, and $\lambda6814.94$. The hfs components for most of these spectral lines were obtained from Johnson et al. (2006), but the components for $\lambda5352.04$ came from Jofré et al. (2017). The solar-normalized abundances for these V and Co lines derived using the *blends* driver are in good agreement with the solar-normalized abundances derived from the V and Co lines that were analyzed with the standard MOOG *abfind* driver. The hfs effects for these lines therefore evidently have a negligible effect on the solar-normalized abundances, and the adopted V and Co abundances quoted in Table 2 are the mean of the abundances derived using the *blends* and *abfind* drivers. We also note that hfs affects mostly lines with larger EWs, which we found to be roughly ≥ 40 mÅ.

For two elements, K and Y, the abundance was derived from the measurements of a single spectral line. In order to obtain the best estimate of the total uncertainty in the abundance for these particular lines, we estimated how the uncertainty in the

EW-measurement affected the uncertainty in the abundance. For simplicity, a minimum-maximum method was used. For both lines, we chose three different continuum placements within the rms scatter of the local continuum, and for each continuum placement made four different measurements of the EW. This gave us a set of 12 EWs for each line in both the Kepler−444 and solar spectra. For each line, the maximum and minimum EW values were used to compute a maximum and minimum $\log(N_X)$. The differences between the maximum and minimum $\log(N_X)$ were adapted as the uncertainties in $\log(N_X)$ and propagated through the computation of the solar-normalized abundances. These uncertainties in the solar-normalized abundances (due to the uncertainty in the EWs) were then added in quadrature to the errors in the abundances due to the stellar parameters, in order to determine the final uncertainties quoted in Table 2. We also note that the sensitivity of the derived abundances to the adopted metallicity is small compared to the sensitivities to T_{eff}, $\log g$, and ξ.

We also determined the Mn abundance as another odd-Z element. Mn is only weakly NLTE dependent, corrections are only 0.003 dex (Bergemann & Gehren 2008), even less than for O, and thus we neglected NLTE effects for Mn. However, we have reliable hfs components (Johnson et al. 2006) for only three Mn lines ($\lambda5432.546$, $\lambda6013.513$, $\lambda6021.819$). We measured other Mn lines that we did not have hfs components for and found a large spread of up to -0.2 dex in the abundances, so we do not consider them to be reliable without hfs corrections. The average of the three lines is given in Table 2. In addition, we attempted to measure Li, but there was no spectral line distinguishable from the continuum noise at $\lambda6707.8$. There were also no discernible spectral lines for the high-excitation N lines at $\lambda7468.3$, $\lambda8216.3$, and $\lambda8683.4$.

The analysis we performed was nearly identical to the analysis of the planet-hosting wide binaries HD 20782/81 (Mack et al. 2014) and HD 80606/07 (Mack et al. 2016). The stellar parameters and relative abundances that we derived for Kepler−444 are summarized in Table 2. The adopted line list, EWs, and line-by-line $\log N$ abundances of each element for Kepler−444 and the Sun are given in Table A.1.

4. Results

4.1. Stellar parameters and abundances

The stellar parameters ($T_{\text{eff}} = 5\,172 \pm 75$ K, $\log g = 4.56 \pm 0.18$, $\xi = 1.64 \pm 0.37$ km s^{-1}, and [Fe/H] $= -0.52 \pm 0.12$) and elemental abundances (Table 2) derived for Kepler−444 are consistent with it being a metal-poor ∼K0 dwarf. The $\log g$ value is identical to the one derived from asteroseismology by Campante et al. (2015), whereas our value for T_{eff} differs from theirs by 126 K. However, the two T_{eff} values still agree within 3σ.

We also note here that given the ≈50-day rotation period of Kepler−444 (see Sect. 4.3), a radius of 0.75 $R_{\odot}$ translates into a maximum $v \sin i$ of ≈0.8 km s^{-1}. This value is considerably lower than both our value for the microturbulence (1.6 km s^{-1}) and the resolution of PEPSI (≈1.3 km s^{-1}). We conclude that the spectral lines of Kepler−444 should not be significantly affected by rotational broadening.

Kepler−444 has significantly enhanced α-abundances. To determine [α/Fe] for Kepler−444, we averaged [O/H], [Mg/H], [Si/H], [Ca/H], and [Ti/H] to obtain a value of [α/Fe] $=$ 0.23. This value agrees well with the value of 0.26 that Campante et al. derived using their values for [Si/H] and [Ti/H].
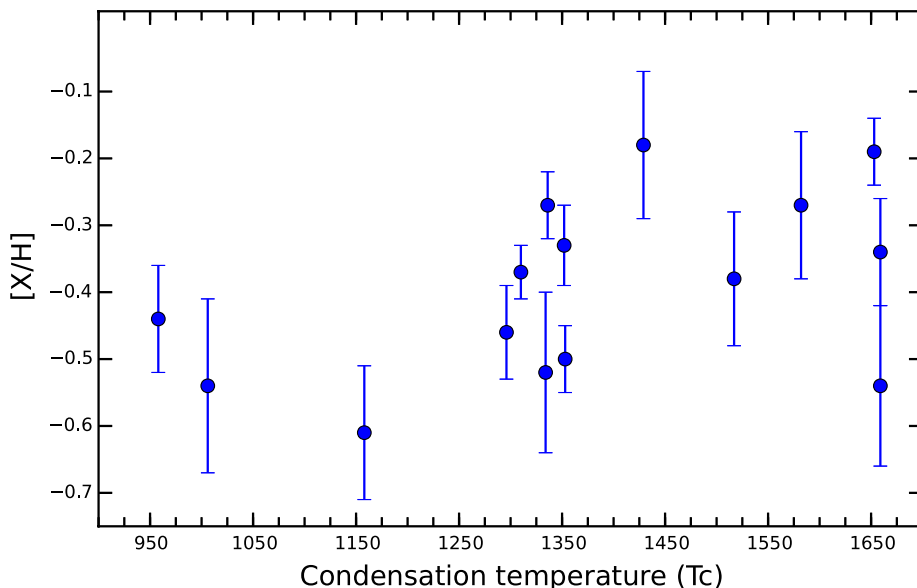
Previous studies (e.g., Meléndez et al. 2009; Ramírez et al. 2010; Schuler et al. 2011; Meléndez et al. 2014) have shown that Sun-like stars tend to show an increase in elemental abundance as a function of elemental condensation temperature, while the Sun itself appears to be depleted in elements with high condensation temperatures, that is, the refractory elements. Since it is these refractory elements that are the main constituents of rocky, terrestrial planets, it has been suggested (Meléndez et al. 2009; Ramírez et al. 2010) that the Sun being depleted in refractory elements may reflect the fact that these elements are locked up in the solar system's rocky planets. Therefore, given that Kepler−444 hosts five rocky planets, we investigated whether its abundances show any particular trend with condensation temperature.

Figure 2 shows the relative abundances of Kepler−444 vs. condensation temperature (T_C) for the refractory elements ($T_C > 950$ K). These relative abundances are the means of the line-by-line differences between $\log N_{\text{Kepler}-444}$ and $\log N_{\text{Sun}}$. For the condensation temperatures, we used the 50% T_C values tabulated in Lodders (2003). There is no evident trend in the abundances as a function of condensation temperature. A simple linear regression fit returns an insignificant positive slope of $+0.00019 \pm 0.00012$ dex/K with a standard fit deviation of 0.11 and chi-square of 0.21. A Pearson correlation gives a coefficient of 0.393, which for a sample size of 15 gives an adjusted correlation coefficient of only 0.07.

In the following subsections, we describe several age indicators that we used to check for consistency with the asteroseismic age of 11 ± 1 Gyr. We also note that while each of the following age indicators have uncertainties greater than that of the asteroseismic age, each indicator does yield an age (~ 10–11 Gyr) that agrees well with the asteroseismic one, and that our main goal is to show that a variety of age indicators consistently produce an old age for Kepler−444.

4.2. Yale-Potsdam Isochrones

Given the spectroscopic $\log g$ and T_{eff} we determined for Kepler−444, we used the Yale-Potsdam isochrones (YaPSI; Spada et al. 2017) to determine a mass and age for Kepler−444. We used the YaPSI models in conjunction with the Monte Carlo Markov chain best-fit search tool BAGEMASS (Maxted et al. 2015). The χ^2 minimization was performed with respect to the available observational constraints on the following parameters: $L/L_\odot$, T_{eff}, $\log g$, and [m/H] (the alpha-enhanced rescaled metallicity; see below). Gravitational settling of He and heavy elements is also taken into account in the YaPSI models; this effect is important for a low-mass, old star such as Kepler−444. For Kepler−444, an initial [m/H] of ≈ -0.30 is indeed required to fit the present value of [m/H] $= -0.4$. Our best-fit solution yields a mass of $M = 0.76\,M_\odot$ and age of 10 ± 1.5 Gyr. These values are in good agreement with those derived by Campante et al. (2015).

In order to take into account the enhancement in α-elements ([α/Fe] ≈ 0.2), we used the scaling relation of Salaris et al. (1993). Essentially, this scaling mimics the effects on the stellar models from the α-enhanced abundances by introducing an effective rescaled metallicity ([m/H]) that is slightly more metal-rich than the spectroscopically determined metallicity ([Fe/H]). These scaling relations are valid for stars that are sufficiently metal-poor (Kim et al. 2002). In the case of Kepler−444, with [α/Fe] ≈ 0.2 and [Fe/H]$=-0.52$, we obtain a rescaled metallicity of [m/H]$=-0.40$; this is the value quoted in Fig. 3. We note that the dashed lines in Fig. 3 represent YaPSI isochrones with the same [m/H] for a range of ages that brackets the best-fit value of 10 Gyr. The shaded gray region is merely intended to guide the eye and highlight the locus defined by these isochrones; it is not a confidence interval.

4.3. Gyrochronology

Mazeh et al. (2015) have determined a rotation period of 49.4 ± 6 days for Kepler−444 from Kepler satellite data. Although the uncertainty in the period is large, it is typical for stars of such long periods in Kepler data, given the ≈ 90-day length of each Kepler quarter. The relatively long period immediately indicates a fairly old star.

Stars of comparable mass to Kepler−444 have rotation periods of ≈ 24 days in the 2.5 Gyr old open cluster NGC 6819 (Meibom et al. 2015), and ≈ 31 days in the 4 Gyr old open cluster M 67 (Barnes et al. 2016). Extrapolation of the Skumanich-type rotation-age relationship to the period of Kepler−444 implies an age slightly in excess of 10 Gyr.
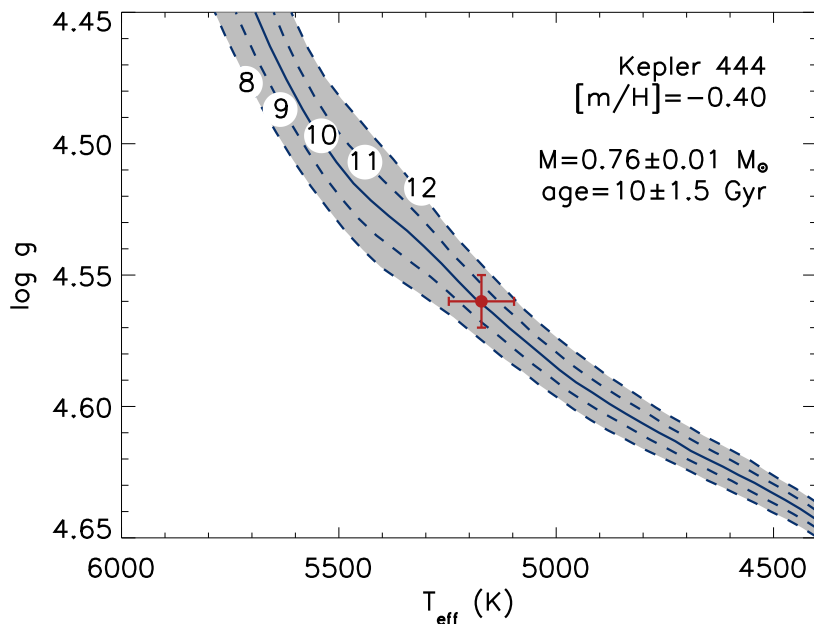
Fig. 3. Kepler−444 H-R diagram. The point with error bars corresponds to the T_{eff} and $\log g$ of Kepler−444. The curves are the isochrones from YaPSI. The numbers in circles indicate the age in Gyr for each isochrone. The solid curve is the best-fit age.

A more precise formulation of gyrochronology, validated by reproducing the mass and age dependencies of rotation in a series of open clusters, including the 4 Gyr old open cluster M 67, is available in Barnes (2010). This formulation yields a gyro age for Kepler−444 of 10.9 ± 2.5 Gyr, where we have used the convective turnover timescales tabulated in Barnes & Kim (2010). The uncertainty in the gyro age is completely dominated by the relatively large uncertainty in the rotation period determination.

The gyro age is thus consistent with the asteroseismic determination, but has larger uncertainties in this particular case.

4.4. [Y/Mg]-clock

We also measured [Y/H] in order to take advantage of the [Y/Mg] age indicator for solar twins that was introduced by Nissen (2015) and further investigated by Tucci Maia et al. (2016). While Kepler−444 is certainly not a solar twin, we thought it would be interesting to see whether [Y/Mg] would yield an age consistent with the asteroseismic age and the other age indicators we employed. We determined that [Y/Mg] $= -0.19$ for Kepler−444, which, using the relation from Tucci Maia et al. (2016), corresponds to an age of ≈ 9 Gyr. Given that their [Y/Mg]-age equation is specifically tuned for solar twins, this age estimate is not too discrepant with the ≈ 10–11 Gyr ages determined from asteroseismology, gyrochronology, and the YaPSI isochrones. Recent studies (Feltzing et al. 2017; Delgado Mena et al. 2017) have shown that thick-disk stars with [Fe/H] < -0.5 do not show a tight correlation between age and [Y/Mg]. Therefore, as a member of the thick-disk population with an [Fe/H] of -0.52, Kepler−444 may be just beyond the limit of the range of applicability for the [Y/Mg]-clock.

4.5. ^{12}C/^{13}C isotope ratio

Finally, we derived an approximate value for the ^{12}C/^{13}C isotope ratio. As a zeroth-order approximation, we measured the equivalent widths of the CN features at 8003.5 Å (due to ^{12}C) and 8004.5 Å (due to ^{13}C). It was not possible to fit a simple Gaussian or Voigt profile to these features, so we integrated the area under the line profile using the Simpson rule integration procedure in MOOG. Repeated adjustments of where the wings of

the spectral line merge with the continuum yielded the following equivalent widths for the two lines respectively; 5.2 ± 0.1 mÅ and 3.0 ± 0.4 mÅ, where the error is the standard deviation in the measurements. Taking the ratio of these two values results in a very low isotope ratio of 1.7, which is consistent with an old age of Kepler−444.

5. Discussion

5.1. C and O abundances of Kepler−444

The C and O abundances of Kepler−444 are consistent with the findings of Bensby & Feltzing (2006) for stars with similar [Fe/H]. In their Fig. 11, it is clear that Kepler−444 lies near the edge of the distribution of stars with [Fe/H] ≈ -0.5, but it is certainly within the overall scatter. However, in Delgado Mena et al. (2010) and Nissen et al. (2014), the C abundance of Kepler−444 falls below the general distribution of stars with [Fe/H] ≈ -0.5. Still, given the scatter in the data for each of these studies, and the relatively few stars with metallicities near -0.5 (varying from 3–10 data points across the three studies), Kepler−444 cannot clearly be considered an outlier, but it has perhaps a relatively low C abundance compared to the stars with similar metallicities, kinematics, and α-enhancement.

In addition, the lack of discrepancy in the relative oxygen abundances ([O/H]) derived from the [O I]-6300 forbidden line and the near-infrared triplet is in agreement with the suggestion from Schuler et al. (2006) that this discrepancy disappears with age. In their studies of the oxygen abundances for the Pleiades, M 34, and Hyades open clusters, as well as for the UMa moving group (Schuler et al. 2004; King & Schuler 2005, and Schuler et al. 2006), they found unexpectedly large O abundances derived from the near-infrared triplet among the K dwarfs in all three open clusters and in the UMa moving group. However, for the Hyades and the UMa moving group (which both have an age of about 600 Myr), the discrepancy was significantly smaller than in the Pleiades and M 34 (which have ages in the range 100−200 Myr). Therefore, the authors posited that the discrepancy may decrease with age, and the nearly identical O abundances derived from the 6300-Å forbidden line and

the near-infrared triplet in Kepler−444 may be the result of this trend. If this trend could be confirmed by studying the O abundances of K dwarfs in a statistical sample of open clusters and moving groups that span a wide range of ages, then this might become a powerful spectroscopic age indicator.

5.2. How Kepler−444 compares to other known metal-poor planet hosts

Adibekyan et al. (2012) showed that metal-poor host stars with small planets are enhanced in α-elements with respect to metal-poor stars without known planets. Furthermore, Adibekyan et al. (2015) showed that small planets tend to prefer host stars with higher [Mg/Si] ratios. Since Kepler−444 falls near the upper limits of the distributions shown in Fig. 4 of Adibekyan et al. (2015) and Fig. 2 of Adibekyan et al. (2012), the enhanced α-abundance ([α/Fe] = 0.23) and the comparatively high value of [Mg/Si] = 0.1 for Kepler−444 are consistent with the findings from Adibekyan et al. (2012; 2015). Thus, Kepler−444 is a member of the growing population of metal-poor host stars that are enhanced in α-elements and possess higher [Mg/Si] than metal-poor non-hosts.

In addition, Adibekyan et al. (2015) suggested that since [Mg/Si] has decreased over time as a result of Galactic chemical evolution, the interior structure and composition of older terrestrial planets, like those in the Kepler−444 system, might be significantly different from the terrestrial planets in the solar system. Compared to the solar system, the mass fraction of Fe may indeed have been considerably smaller, resulting in Earth-mass planets with significantly lower densities and correspondingly larger radii. In the next section, we estimate the possible Fe-core mass fraction of the rocky planets in the Kepler−444 system using the photospheric chemical abundances.

5.3. Estimating the iron core mass fraction from the photospheric abundances

Here we follow the procedure and simplified chemical network used in Santos et al. (2015). This network consists of H, He, C, O, Mg, Si, and Fe because equilibrium condensation models (Lodders 2003; Seager et al. 2007) show that these seven elements are the most important for determining the major species of condensates in the protoplanetary disk, which are H_2O, CH_4, Fe, $MgSiO_3$, and Mg_2SiO_4. Using the photospheric abundance ratios as proxies for the disk abundance ratios, we can relate our derived photospheric atomic abundances for C, O, Mg, Si, and Fe to the disk abundances of the five major condensates listed above. These disk abundances can be converted into mass fractions for each condensate. From these mass fractions, the Fe-core mass fraction of a rocky planet can be estimated by dividing the mass fraction of Fe by the combined mass fractions of Fe and the two magnesium silicates. From our calculations, we would typically expect an Fe-core mass fraction of approximately 24% for the rocky planets in the Kepler−444 system.

When interpreting this value for the Fe-core mass fraction, it is important to keep in mind the following caveats:

(a) This is only a first-order estimate using a simplified chemical network. A full numerical analysis using the photospheric abundances as inputs to determine which molecular and atomic species condense out of the disk should be performed in order to verify this result.

(b) Given that Kepler−444 is metal-poor and α-enhanced, there may be other important disk condensates that are not included in the Santos et al. (2015) simplified chemical network, which is only valid for disk compositions where the Mg abundance is greater than the Si abundance.

(c) From the YaPSI isochrone analysis that we used to determine an age for Kepler−444, we found that due to gravitational settling, Kepler−444 may have initially been ≈0.1 dex more metal-rich. The present-day photospheric abundances of Kepler−444 may therefore be less accurate proxies of the initial disk composition than is typically assumed for stars with solar-type composition.

Keeping these caveats in mind, this estimate of a typical Fe-core mass fraction of ≈24% for terrestrial planets in the Kepler−444 system, which is significantly less than the ∼30% Fe-core mass fraction observed in the solar system and predicted for other systems with solar-type composition (Santos et al. 2015), implies that rocky planets around metal-poor, α-enhanced host stars may tend to be less dense than rocky planets of comparable size around more metal-rich host stars. A recent study (Santos et al. 2017) that estimated the composition of potential planets around a sample of 1 111 stars observed with HARPS (Delgado Mena et al. 2017; Adibekyan et al. 2012), predicts that for old thick-disk stars, the Fe-core mass fraction for rocky planets would be 20−25% (priv. comm. V. Adibekyan).

6. Summary

We have performed a detail chemical analysis of the planet-hosting star Kepler−444 using a high-resolution, high S/N spectrum obtained with the recently commissioned LBT/PEPSI spectrograph. We find that Kepler−444 is α enhanced and metal poor, in agreement with the initial spectroscopic analysis of Campante et al. (2015). Furthermore, using different age indicators, such as the YaPSI isochrones, gyrochronology, and the [Y/Mg] ratio, we find an age of around 10 Gyr for Kepler−444, which is consistent with the 11 ± 1 Gyr that Campante et al. determined from their asteroseismic analysis.

In addition, we note that the good agreement between the relative (to solar) oxygen abundances determined from the [O I]-6300 forbidden line and the near-infrared O I-triplet in Kepler−444 may point toward a potentially powerful spectroscopic age indicator for K dwarfs, if the discrepancy usually observed between these two oxygen abundance indicators in young open clusters is seen to decrease with age in older open clusters.

Finally, we estimate the Fe-core mass fraction of a typical rocky planet in Kepler−444 system by using the photospheric abundances as proxies for the initial chemical composition of the disk. Our estimate of ≈24% suggests that rocky planets in metal-poor α-enhanced systems may tend to be less dense than rocky planets of similar size in more metal-rich systems.

The reduced 1D deep spectra can be downloaded in FITS format from our web page at https://pepsi.aip.de. On demand, we also provide the data prior to continuum rectification.

References

Adibekyan, V. Z., Delgado Mena, E., Sousa, S. G., et al. 2012, A&A, 547, A36
Adibekyan, V. Zh., Figueira, P., Santos, N. C., et al. 2013, A&A, 560, A51
Adibekyan, V., Santos, N. C., Figueira, P., et al. 2015, A&A, 581, L2
Amarsi, A. M., Asplund, M., Collet, R., & Leenaarts, J. 2016, MNRAS, 455, 3735
Barnes, S. A. 2010, ApJ, 722, 222
Barnes, S. A., & Kim, Y.-C. 2010, ApJ, 721, 675
Barnes, S. A., Weingrill, J., Fritzewski, D., Strassmeier, K. G., & Platais, I. 2016, ApJ, 823, 16
Beaugé, C., & Nesvorný, D. 2013, ApJ, 763, 12
Bensby, T., & Feltzing, S. 2006, MNRAS, 367, 1181
Bergemann, M., & Gehren, T. 2008, A&A, 492, 823
Buchhave, L. A., Latham, D. W., Johansen, A., et al. 2012, Nature, 486, 375
Buchhave, L. A., Bizzarro, M., Latham, D. W., et al. 2014, Nature, 509, 593
Campante, T. L., Barclay, T., Swift, J. J., et al. 2015, ApJ, 799, 170
Casagrande, L., Schönrich, R., Asplund, M., et al. 2011, A&A, 530, A138
Cox, A. N. 2000, Allen's Astrophysical Quantities, 4th ed. (New York: AIP Press/Springer)
Dawson, R. I., & Murray-Clay, R. A. 2013, ApJ, 767, L24
Delgado Mena, E., Israelian, G., González Hernández, J. I., et al. 2010, ApJ, 725, 2349
Delgado Mena, E., Tsantaki, M., Adibekyan, V. Zh., Sousa, S. G., Santos, N. C., González Hernández, J. I., & Israelian, G. 2017, A&A, 606, A94
Dressing, C. D., Charbonneau, D., Dumusque, X., et al. 2015, ApJ, 800, 135
Feltzing, S., Howes, L. M., McMillan, P. J., & Stonkutė, E. 2017, MNRAS, 465, L109
Fischer, D. A., & Valenti, J. 2005, ApJ, 622, 1102
Fitzpatrick, M. J., & Sneden, C. 1987, Bull. Am. Astron. Soc., 19, 1129
Ghezzi, L., Cunha, K., Smith, V. V., et al. 2010, ApJ, 720, 1290
Ida, S., & Lin, D. N. C. 2004, ApJ, 616, 567
Hill, J., Green, R. F., Ashby, D. S., et al. 2012, SPIE, 8444, 1
Jofré, P., Heiter, U., Worley, C. C., et al. 2017, A&A, 601, A38
Johnson, J. A., Ivans, I. I., & Stetson, P. B. 2006, ApJ, 640, 801
Kim, Y.-C., Demarque, P., Yi, S. K., & Alexander, D. R. 2002, ApJS, 143, 499
King, J. R., & Schuler, S. C. 2005, PASP, 117, 911
Kupka, F., Piskunov, N., Ryabchikova, T. A., Stempels, H. C., & Weiss, W. W. 1999, A&AS, 138, 119
Lodders, K. 2003, ApJ, 591, 1220
Mack, C. E., III, Schuler, S. C., Stassun, K. G., & Norris, J. 2014, ApJ, 787, 98

Mack, C. E., III, Stassun, K. G., Schuler, S. C., Hebb, L., & Pepper, J. A. 2016, ApJ, 818, 54
Maxted, P. F. L., Serenelli, A. M., & Southworth, J. 2015, A&A, 575, A36
Mazeh, T., Perets, H. B., McQuillan, A., & Goldstein, E. S. 2015, ApJ, 801, 3
Meibom, S., Barnes, S. A., Platais, I., et al. 2015, Nature, 517, 589
Meléndez, J., Asplund, M., Gustafsson, B., & Yong, D. 2009, ApJ, 704, L66
Meléndez, J., Ramírez, I., Karakas, A. I., et al. 2014, ApJ, 791, 14
Mordasini, C., Alibert, Y., Benz, W., & Naef, D. 2009, A&A, 501, 1161
Nayakshin, S. 2017, PASA, 34, 2
Nissen, P. E. 2015, A&A, 579, A52
Nissen, P. E., Chen, Y. Q., Carigi, L., Schuster, W. J., & Zhao, G. 2014, A&A, 568, A25
Piskunov, N. E., Kupka, F., Ryabchikova, T. A., Weiss, W. W., & Jeffery, C. S. 1995, A&AS, 112, 525
Prochaska, J. X., & McWilliam, A. 2000, ApJ, 537, L57
Ramírez, I., Asplund, M., Baumann, P., et al. 2010, A&A, 521, A33
Ramírez, I., Meléndez, J., & Asplund, M. 2014, A&A, 561, A7
Salaris, M., Chieffi, A., & Straniero, O. 1993, ApJ, 414, 580
Santos, N. C., Adibekyan, V., Mordasini, C., et al. 2015, A&A, 580, L13
Santos, N. C., Adibekyan, V., Dorn, C., et al. 2017, A&A, 608, A94
Seager, S., Kuchner, M., Hier-Majumder, C. A., & Militzer, B. 2007, ApJ, 669, 1279
Schuler, S. C., King, J. R., Hobbs, L. M., & Pinsonneault, M. H. 2004, ApJ, 602, L117
Schuler, S. C., King, J. R., Terndrup, D. M., et al. 2006, ApJ, 636, 432
Schuler, S. C., Flateau, D., Cunha, K., King, J. R., Ghezzi, L., & Smith, V. V. 2011, ApJ, 732, 55
Schuler, S. C., Vaz, Z. A., Katime Santrich, O. J., et al. 2015, ApJ, 815, 5
Sneden, C. 1973, ApJ, 184, 839
Sousa, S. G., Santos, N. C., Israelian, G., Mayor, M., & Udry, S. 2011, A&A, 533, A141
Spada, F., Demarque, P., Kim, Y.-C., Boyajian, T. S., & Brewer, J. M. 2017, ApJ, 838, 161
Strassmeier, K. G., Ilyin, I., Jaervinen, A., et al. 2015, Astron. Nachr., 336, 324
Strassmeier, K. G., Ilyin, I., & Steffen, M. 2018a, A&A, 612, A44
Strassmeier, K. G., Ilyin, I., & Weber, M. 2018b, A&A, 612, A45
Takeda, Y. 2003, A&A, 402, 343
Tucci Maia, M., Ramírez, I., Meléndez, J., et al. 2016, A&A, 590, A32
Udry, S., & Santos, N. C. 2007, ARA&A, 45, 397
van Leeuwen, F. 2007, A&A, 474, 653

Appendix A: Spectral lines we measured

Table A.1. Spectral lines we measured, equivalent widths (in mÅ), and abundances.

Ion	λ (Å)	χ (eV)	$\log gf$ (−)	The Sun EW$_\odot$	$\log N_\odot$	Kepler−444 EW	$\log N$
C I	5052.17	7.69	−1.304	37.2	8.53	10.0	8.22
C I	5380.34	7.69	−1.615	21.9	8.52	08.0	8.45
C I	7113.18	8.65	−0.685	22.9	8.49	12.1	8.71
[O I]	6300.30	0.00	−9.717	05.3	8.66	05.4	8.54
O I	7771.94	9.15	+0.369	69.3	8.72	25.2	8.59
O I	7774.17	9.15	+0.223	61.4	8.74	23.1	8.68
O I	7775.39	9.15	+0.001	48.7	8.77	16.9	8.70
Na I	5682.63	2.10	−0.700	98.0	6.27	94.6	5.74
Na I	6154.23	2.10	−1.560	36.6	6.27	35.2	5.89
Na I	6160.75	2.10	−1.260	57.0	6.29	55.4	5.87
Mg I	4730.03	4.35	−2.523	72.8	7.89	76.7	7.52
Mg I	5711.09	4.35	−1.833	105.3	7.61	126.5	7.32
Mg I	6318.72	5.11	−1.945	45.5	7.57	44.6	7.29
Mg I	6319.24	5.11	−2.165	30.8	7.55	30.1	7.30
Mg I	6965.41	5.75	−1.510	24.3	7.29	24.3	7.14
Al I	6696.02	3.14	−1.347	37.3	6.25	46.3	6.05
Al I	6698.67	3.14	−1.647	21.0	6.22	27.2	6.04
Si I	5690.43	4.93	−1.769	53.4	7.53	34.7	7.13
Si I	5701.10	4.93	−1.581	38.5	7.10	26.7	6.79
Si I	5772.15	5.08	−1.358	52.3	7.23	33.9	6.86
Si I	6125.02	5.61	−1.464	31.3	7.46	17.1	7.12
Si I	6142.48	5.62	−1.295	34.1	7.34	19.5	7.02
Si I	6145.02	5.62	−1.310	38.1	7.42	21.3	7.07
Si I	6243.82	5.62	−1.242	46.4	7.49	27.2	7.14
Si I	6244.47	5.62	−1.093	45.2	7.32	26.0	6.96
Si I	6414.98	5.87	−1.035	47.2	7.49	26.0	7.14
Si I	6741.63	5.98	−1.428	16.0	7.37	04.1	6.79
Si I	6848.58	5.86	−1.524	17.0	7.39	07.2	7.01
Si I	7405.77	5.61	−0.313	90.2	7.11	65.5	6.74
K I	7698.98	0.00	−0.170	155.3	5.27	185.3	4.73
Ca I	5867.56	2.93	−1.570	25.5	6.33	29.6	6.02
Ca I	6161.30	2.52	−1.266	63.3	6.30	77.7	5.97
Ca I	6166.44	2.52	−1.142	69.0	6.26	83.7	5.91
Ca I	6169.04	2.52	−0.797	90.9	6.26	108.1	5.85
Ca I	6169.56	2.53	−0.478	110.0	6.21	132.5	5.78
Ca I	6455.60	2.52	−1.340	55.7	6.24	67.6	5.90
Ca I	6493.78	2.52	−0.109	123.8	5.98	148.6	5.53
Ca I	6499.65	2.52	−0.818	85.4	6.18	96.4	5.73
Sc II	6245.64	1.51	−1.030	34.3	3.06	23.9	2.73
Sc II	6604.60	1.36	−1.309	35.1	3.18	24.1	2.83
Ti I	5022.87	0.83	−0.434	72.5	4.79	102.4	4.44
Ti I	5024.84	0.82	−0.602	68.9	4.88	94.4	4.48
Ti I	5866.45	1.07	−0.840	46.8	4.89	76.8	4.62
Ti I	6091.17	2.27	−0.423	14.5	4.93	30.4	4.78
Ti I	6098.66	3.06	−0.010	05.4	4.81	10.5	4.68
Ti I	6258.10	1.44	−0.355	51.6	4.84	77.3	4.53
Ti I	6261.10	1.43	−0.479	48.8	4.90	74.5	4.60
Ti II	5154.07	1.57	−1.750	72.2	5.01	77.7	4.90
Ti II	5336.79	1.58	−1.590	70.6	4.82	59.9	4.45
Ti II	5381.02	1.57	−1.920	57.3	4.87	46.8	4.55
V I	5737.06	1.06	−0.740	12.0	3.98	28.5	3.75
V I	6081.44	1.05	−0.579	13.8	3.85	33.9	3.66
V I	6090.21	1.08	−0.062	32.7	3.85	58.3	3.57
V I	6111.65	1.04	−0.715	11.5	3.89	31.5	3.74
V I	6224.53	0.29	−2.010	05.6	4.08	21.7	3.97
V I	6243.11	0.30	−0.980	29.3	3.90	71.0	3.78

Table A.1. continued

Ion	λ (Å)	χ (eV)	$\log gf$ (−)	The Sun EW$_\odot$	$\log N_\odot$	Kepler−444 EW	$\log N$
V I	6251.83	0.29	−1.340	15.4	3.89	45.9	3.75
Cr I	5702.31	3.45	−0.667	25.4	5.83	23.2	5.37
Cr I	5783.06	3.32	−0.500	32.0	5.68	30.8	5.22
Cr I	5783.85	3.32	−0.295	42.3	5.67	30.8	5.20
Cr I	5787.92	3.32	−0.083	45.4	5.51	44.4	5.03
Cr I	6330.09	0.94	−2.920	26.3	5.61	40.3	5.18
Cr I	7400.25	2.90	−0.111	74.2	5.54	86.1	5.11
Fe I	4779.44	3.42	−2.000	40.5	7.25	39.0	6.77
Fe I	4788.76	3.24	−1.800	65.5	7.29	62.2	6.69
Fe I	5054.64	3.64	−1.900	39.8	7.33	38.3	6.88
Fe I	5322.04	2.28	−2.800	59.8	7.24	58.8	6.61
Fe I	5379.57	3.69	−1.500	60.6	7.33	53.6	6.75
Fe I	5522.45	4.21	−1.600	42.3	7.52	33.5	7.00
Fe I	5543.94	4.22	−1.100	61.5	7.46	52.7	6.91
Fe I	5546.50	4.37	−1.300	50.6	7.58	41.3	7.06
Fe I	5546.99	4.22	−1.900	27.1	7.58	24.8	7.20
Fe I	5560.21	4.43	−1.200	51.3	7.53	39.7	6.98
Fe I	5587.57	4.14	−1.900	38.9	7.69	32.1	7.20
Fe I	5646.68	4.26	−2.500	7.4	7.53	05.0	7.04
Fe I	5651.47	4.47	−2.000	18.9	7.70	12.7	7.20
Fe I	5652.32	4.26	−1.900	26.1	7.64	18.3	7.11
Fe I	5661.35	4.28	−1.700	22.3	7.35	15.4	6.84
Fe I	5667.52	4.18	−1.600	50.4	7.66	36.2	7.04
Fe I	5679.02	4.65	−0.900	58.6	7.58	46.9	7.04
Fe I	5680.24	4.19	−2.600	11.0	7.73	07.8	7.25
Fe I	5731.76	4.26	−1.300	56.9	7.57	46.0	7.01
Fe I	5741.85	4.26	−1.900	31.2	7.64	23.4	7.14
Fe I	5752.03	4.55	−1.200	53.8	7.66	42.7	7.13
Fe I	5775.08	4.22	−1.300	57.9	7.55	47.3	6.98
Fe I	5778.45	2.59	−3.500	22.0	7.44	21.2	6.92
Fe I	5809.22	3.88	−1.800	48.3	7.59	39.1	7.03
Fe I	6079.00	4.65	−1.100	45.9	7.55	32.4	7.00
Fe I	6085.26	2.76	−3.100	42.5	7.64	59.1	7.39
Fe I	6098.24	4.56	−1.900	16.5	7.57	10.0	7.05
Fe I	6151.62	2.18	−3.300	48.3	7.37	49.6	6.80
Fe I	6159.37	4.61	−2.000	12.2	7.56	07.3	7.04
Fe I	6165.36	4.14	−1.500	43.7	7.37	33.8	6.83
Fe I	6187.99	3.94	−1.700	46.1	7.47	36.6	6.92
Fe I	6220.78	3.88	−2.500	19.1	7.58	14.0	7.06
Fe I	6226.73	3.88	−2.200	28.2	7.56	20.5	7.02
Fe I	6229.23	2.85	−2.800	35.7	7.30	32.7	6.76
Fe I	6240.65	2.22	−3.200	47.3	7.31	47.6	6.74
Fe I	6293.92	4.84	−1.700	13.2	7.56	07.4	7.04
Fe I	6380.74	4.19	−1.400	51.2	7.46	40.3	6.90
Fe I	6392.54	2.28	−4.000	17.7	7.53	19.3	7.04
Fe I	6597.56	4.79	−1.100	43.9	7.57	31.6	7.06
Fe I	6608.02	2.28	−4.000	17.0	7.49	19.6	7.04
Fe I	6627.54	4.55	−1.700	27.1	7.62	19.3	7.14
Fe I	6703.57	2.76	−3.200	35.9	7.54	34.3	7.02
Fe I	6710.32	1.49	−4.900	15.1	7.49	18.1	6.96
Fe I	6713.74	4.80	−1.600	20.7	7.62	13.0	7.13
Fe I	6716.22	4.58	−1.900	15.5	7.58	06.2	6.87
Fe I	6725.35	4.10	−2.300	17.9	7.57	11.5	7.02
Fe I	6726.67	4.61	−1.100	25.8	7.10	32.9	6.95
Fe I	6733.15	4.64	−1.600	25.9	7.58	16.2	7.04
Fe I	6739.52	1.56	−4.800	11.3	7.32	14.4	6.83
Fe I	6752.72	4.64	−1.300	35.1	7.49	23.6	6.96
Fe II	4620.52	2.83	−3.300	51.3	7.39	23.9	6.87

Table A.1. continued

Ion	λ (Å)	χ (eV)	$\log gf$ (−)	The Sun EW$_\odot$	$\log N_\odot$	Kepler−444 EW	$\log N$
Fe II	5197.58	3.23	−2.300	79.0	7.36	44.5	6.77
Fe II	5234.62	3.22	−2.300	83.3	7.37	47.0	6.74
Fe II	5264.81	3.23	−3.100	47.1	7.47	20.3	7.00
Fe II	5414.07	3.22	−3.600	28.7	7.56	09.4	7.09
Fe II	5425.26	3.20	−3.400	41.0	7.56	19.3	7.19
Fe II	6149.26	3.89	−2.800	36.2	7.55	10.6	7.02
Fe II	6247.56	3.89	−2.400	51.7	7.47	19.0	6.94
Fe II	7711.72	3.90	−2.700	45.3	7.54	13.8	7.00
Co I	5352.04	3.58	+0.060	25.1	4.57	22.5	4.19
Co I	5301.04	1.71	−2.000	20.8	4.97	30.9	4.66
Co I	5647.23	2.28	−1.560	14.4	4.88	19.5	4.56
Co I	6093.14	1.74	−2.440	09.6	4.99	14.6	4.68
Co I	6814.94	1.96	−1.900	19.3	4.98	27.4	4.67
Ni I	5748.35	1.68	−3.260	28.5	6.19	28.6	5.71
Ni I	5754.66	1.94	−2.330	76.6	6.44	74.5	5.83
Ni I	5760.83	4.11	−0.800	35.1	6.24	23.4	5.75
Ni I	5846.99	1.68	−3.210	22.7	6.00	22.2	5.51
Ni I	6108.11	1.68	−2.450	64.6	6.04	63.6	5.47
Ni I	6111.07	4.09	−0.870	34.2	6.26	22.5	5.77
Ni I	6128.96	1.68	−3.330	24.8	6.15	24.4	5.67
Ni I	6130.13	4.27	−0.960	21.8	6.24	12.6	5.74
Ni I	6133.96	4.09	−1.830	05.8	6.27	04.3	5.92
Ni I	6175.36	4.09	−0.559	48.2	6.21	34.4	5.70
Ni I	6176.81	4.09	−0.260	62.9	6.16	47.3	5.61
Ni I	6177.24	1.83	−3.500	14.8	6.19	13.6	5.70
Ni I	6186.71	4.11	−0.960	30.8	6.29	19.1	5.78
Ni I	6204.60	4.09	−1.100	21.2	6.19	13.1	5.71
Ni I	6223.98	4.11	−0.910	27.5	6.17	17.3	5.68
Ni I	6230.09	4.11	−1.260	21.0	6.36	13.2	5.90
Ni I	6327.59	1.68	−3.150	38.2	6.25	38.6	5.76
Ni I	6370.34	3.54	−1.940	12.8	6.23	09.1	5.80
Ni I	6378.25	4.15	−0.830	31.9	6.22	20.7	5.74
Ni I	6635.12	4.42	−0.820	25.4	6.31	15.8	5.86
Ni I	6643.63	1.68	−2.300	93.9	6.38	93.9	5.74
Ni I	6767.77	1.83	−2.170	78.4	6.11	76.2	5.50
Ni I	6842.04	3.66	−1.480	26.4	6.26	18.3	5.79
Mn I	5432.55	0.00	−4.382	52.2	5.34	79.6	4.83
Mn I	6013.51	3.07	−0.765	87.2	5.36	81.3	4.76
Mn I	6021.82	3.08	−0.537	95.1	5.63	88.5	4.90
Zn I	4722.16	4.03	−0.338	67.9	4.43	52.2	4.02
Zn I	4810.53	4.08	−0.137	71.9	4.35	56.9	3.94
Y II	5200.40	0.99	−0.570	38.0	2.11	22.6	1.57